Element Spectroscopic Imaging of Poly(2-vinylpyridine)-*block*-polyisoprene Microdomains Containing Palladium Nanoparticles

Alexander E. Ribbe,[†,‡,§] **Arimichi Okumura,**[‡,⊥] **Kazumi Matsushige,**[†] **and Takeji Hashimoto***[,‡,§]

Venture Business Laboratory, Kyoto University; Hashimoto Polymer Phasing Project, ERATO, JST; and Department of Polymer Chemistry, Graduate School of Engineering Kyoto University, Kyoto 606-8501, Japan

Received January 2, 2001

ABSTRACT: The distribution of palladium nanoparticles and their influence on the phase separation on a poly(2-vinylpyridine)-*block*-polyisoprene diblock copolymer were visualized by element spectroscopic imaging in the transmission electron microscope. High palladium nanoparticle concentration suppresses the microphase separation of the diblock copolymer, while a comparatively low palladium nanoparticle concentration still induces the microphase separation where the nanoparticles are exclusively located in the poly(2-vinylpyridine) microphase. A careful analysis of the palladium particle distribution revealed that the palladium particles tend to be located close to the interface of the two coexisting microdomains.

1. Introduction

The applicability of metal nanoparticles in the step from micro- to nanotechnology is currently an intensively discussed topic in various scientific fields including electronics, biotechnology, and catalysis.[1,2]

The stabilization of the nanoparticles in order to prevent them from aggregation is one of the essential problems which has to be solved. Some examples of research tackling this problem using surfactants[3−5] or polymers[6−8] have been recently reported. A further challenging problem is the controlled spatial arrangement of them on a substrate or in a polymer matrix. Diblock copolymers, which form various highly ordered morphologies with periodicity on nanometer scale due to microphase separation, have been employed to selectively localize metal nanoparticles in one of the phases[9−17] which in principle enables us to create a periodic spatial arrangement of the particles in a polymer matrix. Besides their influence on the morphology of bulk polymer samples, the incorporation of nanoparticles in polymer micelle solutions is discussed in the literature.[18] Metal vaporization techniques[19] as well as sonochemical preparation methods[20,21] have been described for a wide range of metals as well.

In this paper we report a morphological analysis of the influence of the concentration of palladium nanoparticles embedded in poly(2-vinylpyridine)-*block*-polyisoprene diblock copolymer by means of element-filtered transmission electron microscopy.[22,23] The capabilities of this technique, which is sometimes also called element spectroscopic/specific imaging, provides an elegant way to avoid the standard staining procedures by heavy metal compounds such as OsO_4 or RuO_4. The method has already successfully been used to identify the morphology of diblock copolymers of various kinds.[24−27] The capabilities of this technique are especially helpful in the system discussed here, because the staining agent (OsO_4) which is used conventionally in order to visualize the microdomain structure of the diblock copolymers might cover important information in regard to the spatial distribution of the palladium particles.

Closely related to the diblock copolymer system to be discussed here are studies by Tsutsumi et al.[15] and Okumura et al.[17] which describe the preparation, incorporation, and location control of palladium nanoparticles in a poly(2-vinylpyridine)-*block*-polyisoprene diblock copolymer or in blends of the same diblock copolymer with varying molecular weight. The palladium nanoparticles were reported to be located in the P2VP phase due to their specific interaction with the P2VP-part of a diblock copolymer. A statistical analysis of samples with a very low nanoparticle content was presented and it was shown further that the location of the nanoparticles in the P2VP phase depends on the composition and molecular weights of the diblock copolymers used for the blends.[17] In the following we will compare the there obtained results with the present results on the here discussed samples. In comparing the two results we note that both samples have a comparably high palladium particle content.

2. Experimental Section

2.1. Sample and Sample Preparation. The poly(2-vinylpyridine)-*block*-polyisoprene diblock copolymer (P2VP-*b*-PI) was synthesized by anionic polymerization. Molecular weight of the PI block was determined by GPC to $M_n = 1.42 \times 10^5$ for the PI precursor (using PI calibration) and that of the P2VP block was calculated to be $M_n = 4.3 \times 10^4$ from the mole ratio of isoprene and 2-vinylpyridine units determined from ^{1}H NMR.

To prepare the palladium nanoparticles, 0.05 g of P2VP-*b*-PI and 0.12 g of palladium acetylacetonate ($Pd(acac)_2$) were dissolved in 80 mL of a mixture of benzene and 1-propanol (87/13 vol/vol). This solution was refluxed under N_2 atmosphere

---

* To whom correspondence should be addressed at Kyoto University.

[†] Venture Business Laboratory, Kyoto University.

[‡] Hashimoto Polymer Phasing Project, ERATO, JST.

[§] Department of Polymer Chemistry, Graduate School of Engineering, Kyoto University.

[⊥] Current address: Technical Center, Daicel-Degussa, Ltd. 1239, Shinzaike, Aboshi-ku, Himeji, Hyogo 671-1239, Japan.

10.1021/ma0100091 CCC: $20.00

Table 1. Energy Loss of the Onset of the Element Edge of Nitrogen and Palladium, ΔE, Energy Width dE, and Onset Energy ΔE_o of the Pre- and Postimages Used for Determination on the Net Element Distribution Images

element	shell	ΔE (eV)	dE (eV)	$\Delta E_o^{\mathrm{pre-1}}$ (eV)	$\Delta E_o^{\mathrm{pre-2}}$ (eV)	$\Delta E_o^{\mathrm{post}}$ (eV)
N	K	−401	30	−361	−381	−421
Pd	$N_{2,3}$	−51	8	−37	−45	−61

at 85 °C for 48 h, and a homogeneous colloidal dispersion of Pd nanoparticles was obtained. The particles were precipitated in acetone and subsequently centrifuged in benzene. For the experiments both the precipitate (i) and the remaining solution (ii) were used: (i) The precipitate, coded Pd_{high}(P2VP-*b*-PI), contains mainly P2VP-*b*-PI which is adsorbed onto the Pd-particles and some free P2VP-*b*-PI. (ii) The solution, code Pd_{low}(P2VP-*b*-PI), contains a larger fraction of free P2VP-*b*-PI compared to Pd_{high}(P2VP-*b*-PI) besides some Pd particles carrying P2VP-*b*-PI molecules.

The samples of Pd_{high}(P2VP-*b*-PI) and Pd_{low}(P2VP-*b*-PI) for transmission electron microscopic investigations were obtained via solvent casting from 5 wt % benzene solutions at 30 °C. Thus obtained bulk specimens were ultramicrotomed at −100 °C with a diamond knife to sections of about 50 nm thickness using Reichert-Nissei Ultracut-S Ultramicrotome.

2.2. Element Spectroscopic Transmission Electron Microscopy. Element spectroscopic measurements were done with a JEOL-2000FX equipped with a GATAN electron energy loss filter and imaging system at an acceleration voltage of 200 kV. All element distribution images were acquired using the so-called three-window method, which uses two background images acquired in front of the element edge (preedge images) and one image acquired after the element edge (postedge image) to calculate a net element distribution via extrapolation. The basis for the contrast enhancement of the postedge image via subtraction of a background image is given by eq 1.[22,23]

$$I = A \exp(-r\Delta E) \qquad (1)$$

Using the two preedge images at an onset energy of $\Delta E_o^{\mathrm{pre-1}}$ and $\Delta E_o^{\mathrm{pre-2}}$, in the energy loss spectrum, the parameters A and r can be calculated[23] and a background image is generated via extrapolation for the element of our interest with energy loss onset at $\Delta E_o^{\mathrm{post}}$. The energy width and position, i.e., energy loss, of this background image are the same like the postedge image. This background image is subtracted from the postedge image to give a net element distribution image which is sometimes also called element mapping. Owing to the background subtraction, artifacts arising from sample thickness variations or contaminations are widely removed, and in the optimum case only the location of the probed element shows enhanced intensity on the net element distribution image.

In the here examined samples, the elements of interest are palladium and nitrogen, associated with P2VP, and net element distribution images were obtained using the energy losses summarized in Table 1.

3. Results and Discussion

3.1. Electron Energy Loss Spectroscopy. Figure 1 shows the electron energy loss (EEL) spectra of both Pd_{low}(P2VP-*b*-PI) and Pd_{high}(P2VP-*b*-PI). The two samples contain the same elements and only differ in the amount of palladium. The EEL spectra are obtained by averaging over an circular-shaped area with a diameter of about 500 nm, which is much larger than the smallest structural units, i.e., phase-separated domain structures of the block copolymer or size of nanoparticles. The following interpretation is the same for both samples.

Part a shows the zero loss region where the intensity maximum at energy loss $\Delta E = 0$ eV corresponds to unscattered electrons passing through the sample. The maximum at about $\Delta E = 22$ eV reflects plasmons, i.e., the inelastic scattering caused by σ- or π-valence electrons due to covalent bonding of the atoms in the sample. The small maximum with onset at an energy loss of about $\Delta E = 37$ eV is caused by the palladium $N_{2,3}$-edge with a maximum at $\Delta E[Pd(N_{2,3})] = 51$ eV of the palladium particles and was used for imaging as described below.

The palladium M-edge at $\Delta E[Pd(M_{4,5})] = 335$ eV described later is not usable for imaging purposes as this edge sits too close to the very strong carbon K-edge, having an onset at $\Delta E[C(K)] = 284$ eV and a maximum at $\Delta E = 305$ eV, and makes an extrapolation of the background and therefore the determination of the background image impossible. Therefore, despite the fact that the range between the plasmon peak maximum and the onset of the $Pd(N_{2,3})$-edge usable for background calculation is very narrow, the $Pd(N_{2,3})$-edge at $\Delta E[Pd(N_{2,3})] = 37$ eV was chosen for imaging. The plasmon intensity is still very high and has a very small energy width d$E = 8$ eV (see Table 1), which is sufficient enough to calculate a background image for the $Pd(N_{2,3})$-edge.

Figure 1b shows the core loss region from $\Delta E = 250$ eV to $\Delta E = 600$ eV. The strong signal with a maximum at $\Delta E = 305$ eV is caused by the carbon-K-edge at $\Delta E[C(K)] = 284$ eV of the carbon of the polymer backbone. The subsequent shoulder at $\Delta E = 330$ eV is caused by plural scattering as a result of the sample thickness which is in the range or larger than the mean free path of inelastic scattering, which is for the here given conditions about 30 nm. The area after this shoulder ($\Delta E < 335$ eV) is important for understanding the contrast generation of the nitrogen distribution images in the following sections. As mentioned above, the palladium has a further strong adsorption edge at $\Delta E[Pd(M_{4,5})] = 335$ eV. This edge is characterized by an onset at $\Delta E = 335$ eV and a delayed maximum at about $\Delta E = 400$ eV.[28] To better visualize this edge, the background-corrected spectrum in this area is magnified in Figure 1c. The background corrections are achieved by fitting the area before the onset of the respective peaks by using eq 1, interpolating over the peak area, and subsequently subtracting the interpolated curve from the original data. One can clearly see that the peak goes through a maximum at about $\Delta E = 400$ eV and a smaller peak combination at $\Delta E = 530$ eV, which corresponds to a minor absorption of the $Pd(M_3)$-edge at $\Delta E = 531$ eV and $Pd(M_2)$-edge at $\Delta E = 559$ eV. The data are consistent with the spectrum obtained for pure palladium found in the literature.[28]

Owing to the above-described strong scattering of the palladium, the signal of the nitrogen-K-edge at $\Delta E[N(K)] = 401$ eV of the nitrogen contained in the poly(2-vinylpyridine) is hidden under the palladium $M_{4,5}$-edge and cannot be surely identified in the spectrum.

3.2. Element Spectroscopic Imaging. The bright field, nitrogen distribution, and palladium distribution images of the as-cast diblock copolymer samples Pd_{low}(P2VP-*b*-PI) and Pd_{high}(P2VP-*b*-PI) are given in Figure 2 and Figure 5, respectively.

3.2.1. Pd_{low}(P2VP-*b*-Pi). The image series in Figure 2, corresponding to Pd_{low}(P2VP-*b*-PI) containing low palladium particle concentration, shows a lamellar morphology due to the microphase separation of the poly(2-vinylpyridine) and polyisoprene as observed for the pure diblock copolymer. Figure 2a shows the bright

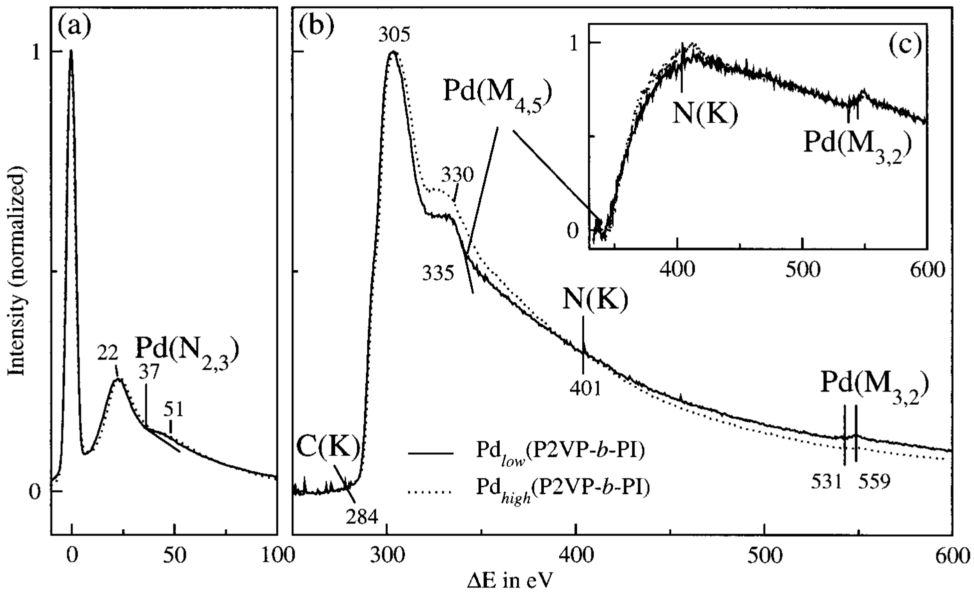

Figure 1. Electron energy loss (ΔE) spectra of Pd $_{\text{low}}$(P2VP-*b*-PI) (solid line) and Pd$_{\text{high}}$(P2VP-*b*-PI) (dotted line). Part (a) shows the zero-loss area with the zero-loss peak at ($\Delta E = 0$ eV), the plasmon peak at ($\Delta E = 22$ eV) and the palladium $N_{2,3}$-edge at about $\Delta E = 50$ eV. Part (b) shows the core-loss region with the carbon K-edge at $\Delta E = 284$ eV and the palladium $M_{4,5}$-edge at $\Delta E = 335$ eV as well as the palladium M_3-edge and palladium M_2-edge at $\Delta E = 531$ eV and $\Delta E = 559$ eV, respectively. Part (c) is the background corrected spectrum obtained via extrapolation and background subtraction at the palladium $M_{4,5}$-edge at $\Delta E = 335$ eV.

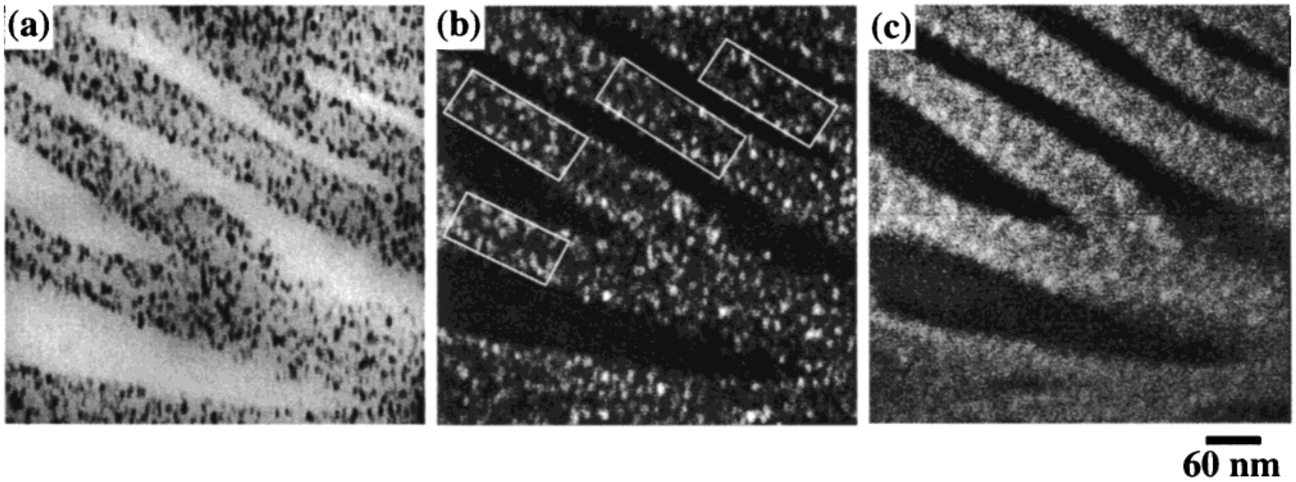

Figure 2. Net element distribution images of Pd$_{\text{low}}$(P2VP-*b*-PI). Bright field (a) recorded at zero loss energy. The palladium distribution (b) and nitrogen distribution (c) images obtained via the three-window method discussed in the text.

field image at zero loss energy. The contrast on this image is caused by the difference in elastic scattering behavior of the different components for which coulomb attraction of the core to the incoming electrons are responsible (classical contrast generation in the TEM). As the palladium is the element with the highest atomic number it causes the strongest scattering and the palladium particles therefore appear as dark spots on the bright field image. From the bright field image it is, however, crucial to determine the location of the two polymer components, P2VP and PI. The atomic composition and density of the two polymers are too similar to cause a sufficient contrast. Although the phase containing the palladium particles seems to be darker compared to the palladium-free phase, one cannot distinguish between the two polymers in this image. When comparing the nitrogen distribution image in Figure 2c with the palladium distribution image given in Figure 2b, it becomes obvious that only the poly(2-vinylpyridine) phase contains palladium particles.

The palladium particles show enhanced intensity in the nitrogen distribution image as well, which is due to the intensity overlap of the palladium $M_{4,5}$-edge and the nitrogen K-edge as described in the previous section and hence to incomplete subtraction of the palladium edge from the nitrogen edge. The overlap of the nitrogen K-edge at $\Delta E[\mathrm{N(K)}] = 401$ eV with the palladium $M_{4,5}$-edge at $\Delta E[\mathrm{Pd}(M_{4,5})] = 335$ eV causes the palladium particles to be visualized on the nitrogen mapping. For the following analysis of the palladium particle distribution, this overlap is not important as we only need the palladium particle distribution image in part b. The nitrogen distribution image is used to determine the lamella interface on the palladium distribution image.

The Pd particles have an average size of 4−5 nm in diameter. To investigate the spatial distribution of the palladium particles in the P2VP domains, a careful image analysis of the Pd particle distribution was done using the areas marked by white rectangles in Figure 2. This image analysis, which is schematically il-

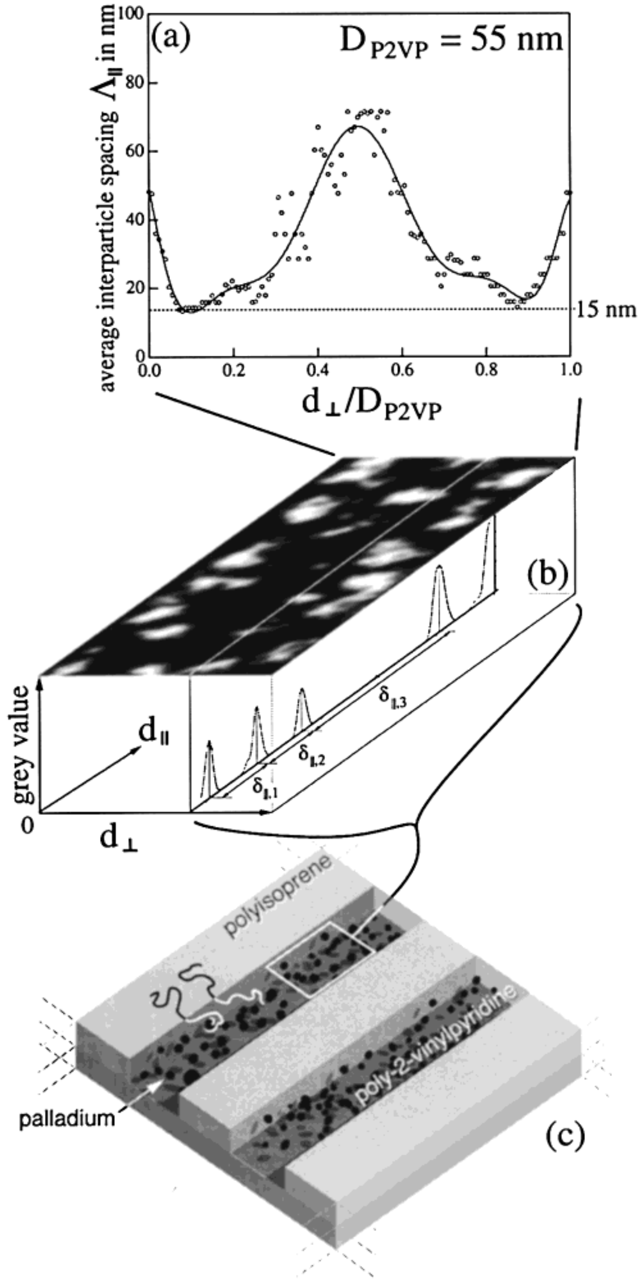

Figure 3. Schematic illustration of the image-analysis method for the determination of the average particle distance as a function of distance $d_{\perp}$ from the lamella interface at an origin 0 along the lamella normal, for the calculation of a particle density profile along the lamellar normal. (a) Average interparticle spacing $\Lambda_{\|}$ in nm of the Pd particles as a function of distance $d_{\perp}$ from the lamellar interface along the lamella normal reduced by the average thickness of the P2VP lamellae, D_{P2VP}. (b) Method used to calculate $\Lambda_{\|}$ from the spacing $\delta_{\|,k}$ along the curvilinear line at a distance $d_{\perp}$ from the interface. (c) Schematic illustration of the morphology of the system.

lustrated in Figure 3, was done by determination of the average palladium particle spacing $\Lambda_{\|}$ along the curvilinear line parallel to the lamellar interface and at a distance $d_{\perp}$ from the interface, which is directly a measure for the local particle density as a function of $d_{\perp}$ in the direction along the lamellar normal. The calculations were done using the gray value profiles corresponding to the location of the palladium particles along the lines at a distance $d_{\perp}$ perpendicular to the lamellar interface and measuring the distance ($\delta_{\|,k}$ with k being a running index) between the intensity maxima of the profiles which directly corresponds to the location of the palladium particles (Figure 3b). According to the sketch in Figure 3, the average particle spacing $\Lambda_{\|}(d_{\perp})$ at a given distance $d_{\perp}$ from the interface can be defined according to eq 2

$$\Lambda_{\|}(d_{\perp}) = \frac{\sum_{k=1}^{n-1} \delta_{\|,k}(d_{\perp})}{n-1} \tag{2}$$

where n is the number of particles along the line at a distance $d_{\perp}$ and $\delta_{\|}(d_{\perp})$ is the spacing between the respective palladium particles. Figure 3b shows one area of four areas of the palladium distribution images, which were marked in Figure 2 and used for the calculations. Figure 3a corresponds to the average of all four areas. The sketch in Figure 3c shows the corresponding morphology model.

As evident from Figure 3a, the palladium particles are not randomly distributed throughout the poly(2-vinylpyridine) phase but enriched close to the lamellar interface. The maximum density, i.e., minimum palladium particle spacing, is observed at a distance of 4−5 nm from the lamellar interface. The lowest density is observed in the middle of the P2VP lamella.

The results obtained in Figure 3a can schematically be illustrated by Figure 4a and can be understood using the model depicted in Figure 4b. The average degree of polymerization of the P2VP blocks of free P2VP-*b*-PI copolymer and that of P2VP coordinating the palladium particles (Pd-P2VP) are identical. Further only a part of the P2VP blocks is coordinated to the palladium particle and the coordination of the Pd particles occurs more or less uniformly along the P2VP blocks.[29] It therefore becomes clear that the average end-to-end vector of Pd-P2VP ($\vec{r}_{Pd-P2VP}$) is always smaller than the average end-to-end vector of free P2VP ($\vec{r}_{P2VP}$), $|\vec{r}_{Pd-P2VP}| < |\vec{r}_{P2VP}|$ (see Figure 4b). This means that free P2VP block chains tend to compensate the density dip of the P2VP segments of Pd-P2VP block chains at around the center of the P2VP lamellae.

Recently, an approach to quantify the spatial distribution of the palladium particles in similar samples was reported by Okumura et al.,[17] which was based on the measurement of the average distance of the nanoparticles from the lamellar interface. Three different cases have been discussed: (i) The molecular weight of the P2VP block of the PI-*b*-P2VP diblock copolymer coordinating the palladium nanoparticles is (i) smaller, (ii) the same, and (iii) larger than the P2VP blocks of the PI-*b*-P2VP copolymers free from the particles that control the microdomain space for the Pd-(PI-*b*-P2VP).

The sample discussed here corresponds to case (ii) above, where the free and coordinating polymers have identical molecular weight. In our case, however, the palladium particle concentration is much higher or the ratio of free PI-*b*-P2VP to Pd(PI-*b*-P2VP) is much smaller than in case (ii) above. As mentioned above, the average end-to-end distance of the P2VP block that coordinates the particles is shortened compared to that of the free P2VP block. If this is the case, this effect tends to shift the situation of the particle location in our sample toward that of case (i) where the length of the P2VP block that coordinates the particles was much shorter than that of the free P2VP block. In that case the palladium particles are preferably located close to

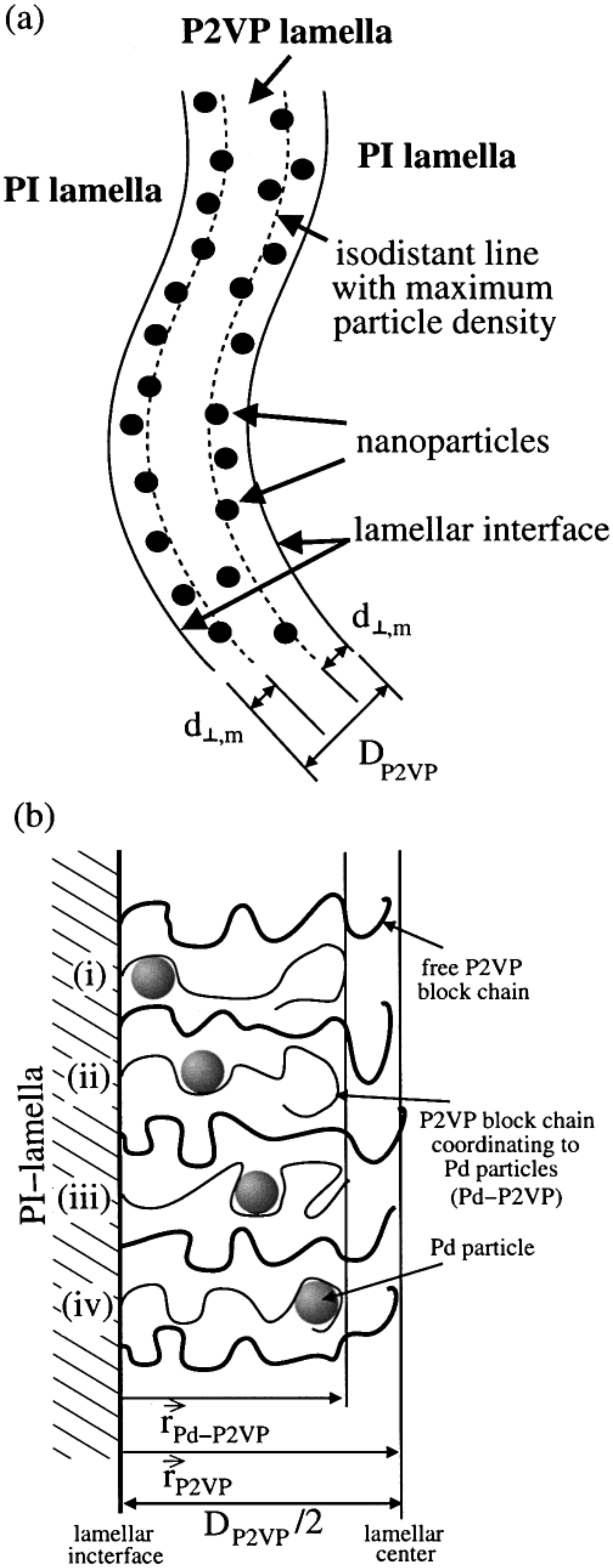

Figure 4. (a) Schematic presentation of the results obtained in Figure 3a and illustration of the principle of isodistant lines from the domain interface for the determination of the palladium particle distribution in the P2VP phase. (b) Model illustrating the influence of the palladium nanoparticles on end-to-end distance of the P2VP blocks. Situations (i) and (iv) are equally probable. $\vec{r}_{P2VP}$ and $\vec{r}_{Pd-P2VP}$ are the average end-to-end vector of free P2VP (thick line) and P2VP coordinated to Pd (thin line), respectively.

the lamellar interface.[17] This explains nicely the enrichment of the palladium particles close to the interface in our sample, similarly to case (i).

There is no discrepancy between the palladium particle distribution for case (ii) presented by Okumura et al.[17] and the results presented here. Owing to the very low palladium particle concentration in the case of Okumura et al., only a few data points were available in regard to the particle positions, introducing a larger error or noise in their probability density distribution. Although not immediately visible, a close observation tends to show that their palladium particles distribution shows a tendency toward an enrichment near the lamellar interface, which is consistent with our results.

3.2.2. Pd $_{\mathbf{High}}$(P2VP-*b*-Pi). The bright field image as well as the palladium and nitrogen distribution images of the P2VP-*b*-PI diblock copolymer containing high palladium particle concentration are given in Figure 5. The dark dots on the bright field image (Figure 5a) and the bright dots on the palladium distribution image (Figure 5b) are complementary and identify those spots as the palladium nanoparticles.

The determination of the average particle spacing was done using the 2D-Fourier transform (FT) of the palladium particle distribution image (Figure 5b). As visible from Figure 5d, the 2D-FT spectrum is not circular but ellipsoidal, indicating a direction-dependent particle distribution. This elongation is caused by preferential orientation of the Pd particles caused by shearing effects during sample preparation, i.e., solvent casting and ultramicrotomy. The average particle spacing was determined to be about 10 nm by averaging the minimum and maximum interparticle spacings, obtained from the peak positions of the 2D-FT profiles along the white lines shown in Figure 5d. The Pd particles have an average diameter of 4−5 nm like those of sample Pd_{low}(P2VP-*b*-PI), revealing evidence that the particles are stabilized by P2VP blocks even at high concentrations.

The nitrogen distribution image obtained at the same sample position like that in Figure 5a,b is shown in Figure 5c. The intensity distribution of the nitrogen distribution image corresponds qualitatively to the contrast observed on the palladium distribution image, or in other words, the nitrogen distribution shows high intensity at the same locations as the palladium distribution images. Owing to the reasons discussed in the previous section, the palladium particles show enhanced intensity on the nitrogen distribution image as well, which gives another possible interpretation on why the nitrogen distribution shows high intensity at the same location as the palladium distribution, in addition to another possible interpretation to be discussed below. Therefore, the interpretation of the location of the nitrogen, i.e., the P2VP, has to be done very carefully. The most obvious difference between this system and the above-described system Pd_{low}(P2VP-*b*-PI) is the absence of the microphase separation with long range order, i.e., no lamellar morphology. These pieces of information allow the following interpretation:

When the Pd particle concentration increases, free P2VP-*b*-PI blocks, which are responsible for formation of the well-defined microdomain structures, inevitably decrease in concentration. At the same time, free space between the Pd particles tend to decrease, due to the interparticle attractions, and consequently the particles coordinated and stabilized by the block chains tend to

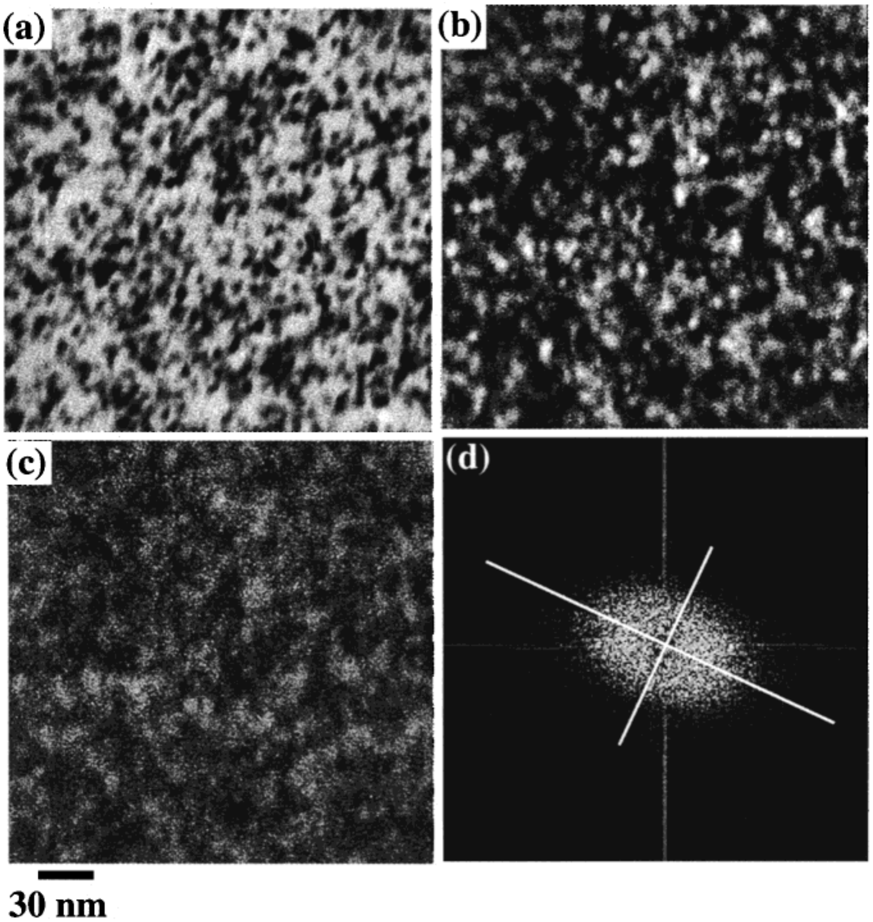

Figure 5. Net element distribution images of Pd_{high} (P2VP-*b*-PI). Bright field (a) was recorded at zero loss energy. The palladium distribution (b) and nitrogen distribution (c) images were obtained via the three-window method. Part (d) is the 2D-Fourier transform of the palladium particle distribution image depicted in part (b).

form aggregates in which the P2VP may be segregated around the particles and intervene in the interstitial region of the particles. This gives the second possible interpretation on why the nitrogen distribution image is similar to that of Pd. The PI blocks may be segregated outside these P2VP domains as coronar chains. In fact, the average interparticle spacing of Pd_{high}(P2VP-*b*-PI) (10 nm) is smaller than the minimum spacing of 15 nm for Pd_{low}(P2VP-*b*-PI) from the analysis leading to the plot in Figure 3a. Thus, microphase separation may occur between the aggregates of the Pd particles intervened by P2VP blocks and the PI coronar blocks emanating from the aggregates. The two phases composed of Pd particles plus P2VP blocks and the coroner PI blocks may tend to form a distorted bicontinuous structure in three-dimensional space, which makes a clear-cut identification of the microdomain structure difficult under the TEM method employed. The detailed morphological study on the two-phase structure deserves future work.

4. Concluding Remarks

In this paper we just used small areas of the TEM image obtained via Pd element mapping for the analysis of the particle distribution. Using larger areas, one can use 1-dimensional Fourier transformation to determine the average particle spacing $\Lambda_{\|}(d_{\perp})$ at $d_{\perp}$ which could be used for automation of such an image analysis. As depicted in the sketch in Figure 4, the method is not restricted to straight lamellar morphologies but can certainly be applied also to evaluate undulating lamellar via determination of the above-mentioned 1-dimensional Fourier transformation along isodistance lines parallel to the lamellar interface. The realization will be a computational problem.

We presented a detailed analysis of the distribution of palladium nanoparticles stabilized by PI-*b*-P2VP and embedded in the matrix of the same block copolymer. Due to specific interactions of the P2VP blocks to the palladium nanoparticles, the particles are exclusively located in P2VP lamellae in a lamellar microphase separated morphology when having low palladium particle content. This could conclusively be shown using the power of the element specific imaging technique in the TEM. A detailed analysis of the palladium particle distribution within the P2VP lamellae further showed that the palladium particles are not randomly distributed in the P2VP lamellae but tend to be located closer to the lamellar interface. High palladium particle content does not allow evolution of a clear-cut microphase-separated morphology of the block copolymer but leads to a random distribution of Pd particles which tend to form interconnected aggregates intervened by P2VP blocks.

References and Notes

(1) Schmid, G., Ed. *Colloidals and Cluster*; VCH Press: New York, 1995.
(2) Timp, G., Ed. *Nanotechnology*; Springer: New York, 1999.
(3) Toshima, N.; Takahashi, T. T. *Bull. Chem. Soc. Jpn.* **1992**, *65*, 400.
(4) Brust, M.; Walker, M.; Bethell, D.; Schiffrin, D. J.; Whyman, R. *J. Chem. Soc., Chem. Commun.* **1994**, 801.

(5) Pileni, M. P. *Langmuir* **1997**, *13*, 3266.
(6) Yonezawa, T.; Toshima, N. *J. Chem. Soc., Faraday Trans.* **1995**, *91*, 4111.
(7) Antonietti, M.; Wenz, E.; Bronstein, L.; Seregina, M. *Adv. Mater.* **1995**, *7*, 1000.
(8) Spatz, J. P.; Mössmer, S.; Möller, M. *Chem. Eur. J.* **1996**, *3*, 1552.
(9) Ng Cheong Chan, Y.; Craig, G. S. W.; Schrock, R. R.; Cohen, R. E. *Chem. Mater.* **1992**, *4*, 244.
(10) Saito, R.; Okamura, S.; Ishizu, K. *Polymer* **1993**, *34*, 1184.
(11) Nakao, Y. *J. Colloid Interface Sci.* **1995**, *171*, 386.
(12) Tamai, H.; Sakurai, H, Hirota, Y.; Nishiyama, F.; Yasuda, H. J. *Appl. Polym. Sci.* **1996**, *56*, 441.
(13) Fogg, D. E.; Radzilowski, L. H.; Blanski, P.; Schrock, R. R.; Thomas, E. L. *Macromolecules* **1997**, *30*, 417.
(14) Zehner, R. W.; Lopes, W. A.; Morkved, T. L.; Jaeger, H.; Sita, L. R. *Langmuir* **1998**, *14*, 241.
(15) Tsutsumi, K.; Funaki, Y.; Hirokawa, Y.; Hashimoto. T. *Langmuir* **1999**, *15*, 5200.
(16) Hashimoto, T.; Harada, M.; Sakamoto, N. *Macromolecules* **1999**, *32*, 6867.
(17) Okumura, A.; Tsutsumi, K.; Hashimoto, T. *Polymer J.* **2000**, *32*, 520.
(18) Moessmer, S.; Spatz, J. P.; Moeller, M.; Aberle, T.; Schmidt, J.; Burchard, W. *Macromolecules* **2000**, *33*, 4791.
(19) Trivino, G. C.; Klabunde, K. J.; Dale, E. B. *Langmuir* **1987**, *3*, 986.
(20) Gutierrez, A.; Henglein, A. *J. Phys. Chem.* **1987**, *96*, 6687.
(21) Mizukoshi, Y.; Okitsu, K.; Maeda, Y.; Yamamoto, T.; Oshima, R.; Nagata, Y. *J. Phys. Chem.* **1997**, *36*, 77033.
(22) Egerton, R. F. In *Electron Energy Loss Spectroscopy in the Transmission Electron Microscope*; Plenum Press: New York, 1996.
(23) Reimer, L. In *Energy-Filtering Transmission Electron Microscopy*; Springer Series in Optical Sciences, Vol. 72; Springer: Berlin, 1995.
(24) Kunz, M.; Moeller, M.; Cantow, H.-J. *Makromol. Chem., Rapid Commun.* **1987**, *8*, 401.
(25) Eisenbach, C. D.; Ribbe, A.; Guenther, C. *Makromol. Chem., Rapid Commun.* **1994**, *15*, 395.
(26) Tanaka, Y.; Hasegawa, H.; T. Hashimoto, T.; Ribbe, A. E.; Sugiyama, K.; Hirao, A.; Nakahama, S. *Polymer J.* **1999**, *31*, 989.
(27) Ribbe, A. E.; Hayashi, M.; Weber, M.; Hashimoto, T. *Macromolecules* **2000**, *33*, 2786.
(28) EELS-Atlas; Part of handbook for Gatan EEL-Spectrometer, Gatan Inc.
(29) Hashimoto, T.; Tanabe, D.; Okumura, A., to be submitted.

MA0100091